

# Non-LTE line-formation for hydrogen revisited

Norbert Przybilla<sup>1</sup>

*Institute for Astronomy, 2680 Woodlawn Drive, Honolulu, HI 96822, USA*

przybilla@sternwarte.uni-erlangen.de

and

Keith Butler

*Universitätssternwarte München, Scheinerstraße 1, D-81679 München, Germany*

butler@usm.uni-muenchen.de

## ABSTRACT

We discuss aspects of non-LTE line formation for hydrogen in early-type stars. We evaluate the effect of variations in the electron-impact excitation cross sections in model atoms of differing complexity by comparison with observation. While the Balmer lines are basically unaffected by the choice of atomic data, the Paschen, Brackett and Pfund series members allow us to discriminate between the different models. Non-LTE calculations based on the widely-used approximation formulae of Mihalas, Heasley & Auer and of Johnson fail to simultaneously reproduce the optical and IR spectra over the entire parameter range. The use of data from *ab-initio* calculations up to principal quantum number  $n \leq 7$  largely solves the problem. We recommend a reference model using the available data. This model is of general interest because of the ubiquity of the hydrogen spectrum.

*Subject headings:* atomic data – line: formation – stars: early-type – stars: fundamental parameters

## 1. Introduction

The quantitative interpretation of the hydrogen line spectrum is one of the foundations of modern astrophysics. Being the most abundant and most basic element in the universe

---

<sup>1</sup>present address: Dr. Remeis-Sternwarte Bamberg, Sternwartstraße 7, D-96049 Bamberg, Germany

hydrogen imprints its signature on the spectra of the majority of astronomical objects. The analysis of these line features allows us to determine the physical properties of stars, nebulae and accretion phenomena. For decades the focus was on the first members of the Balmer series, easily accessible from the ground, with many studies concentrating on understanding, verifying and improving the modelling of these key indicators.

In the meantime developments in detector technology have opened the infrared (IR) window to routine observation, in some bands from the ground, in its entirety from space. IR observations will gain in importance in the future as the next generation of ground-based large telescopes and the next large space telescope will also be operating in this wavelength range. This development is driven mainly by a change of focus to the high- $z$  universe, but it will also allow local objects in otherwise inaccessible environments to be studied, e.g. ultra-compact H II regions, the Galactic centre and dust-enshrouded nearby starburst galaxies. The Brackett and Pfund lines are important diagnostics at these wavelengths. It is natural to ask whether the present modelling is in similar good shape for their quantitative interpretation as it is for the Balmer lines.

The present work therefore addresses several aspects of non-LTE line formation for hydrogen in early-type stars. The next two sections are dedicated to finding a reference H I model atom in order to provide a diagnostic for both visual and IR spectra. This is done by testing different implementations by comparing with observation. The resulting set of reference data is, of course, of much broader interest than for stellar analyses alone. Relevant data from new *ab-initio* computations for electron-impact excitation of hydrogen are presented in an appendix.

## 2. Model calculations

### 2.1. Model atmospheres and programs

The line-formation computations are carried out using two methods. For main sequence stars of spectral types later than O and BA-type supergiants a hybrid approach is chosen. Based on hydrostatic, plane-parallel, line-blanketed LTE models calculated with the ATLAS9 code (Kurucz 1993) the non-LTE computations are performed using DETAIL and SURFACE (Giddings 1981; Butler & Giddings 1985). The coupled radiative transfer and statistical equilibrium equations are solved with the former and the emergent flux computed with the latter. This line-formation package has undergone significant modifications recently, most notably through the inclusion of an ALI scheme (using the treatment of Rybicki & Hummer 1991). Line-blocking is realised by considering Kurucz' ODFs (Opacity Distribution

Functions).

For the modelling of early B and O-type stars we use the non-LTE model-atmosphere/line-formation code FASTWIND (Santolaya-Rey, Puls & Herrero 1997) which accounts for spherical extension and hydrodynamic mass-outflow. It has been recently updated to include an approximate treatment of non-LTE line-blocking/blanketing (Puls et al. 2003).

## 2.2. Atomic data

The two-body nature of the hydrogen atom allows the radiative data to be obtained analytically. On the other hand, excitation and ionization processes involving a colliding particle require a numerical solution of the resulting three-body Coulomb problem. A number of quantum-mechanical *ab-initio* calculations exist for excitation via electron collisions which reproduce the few measurements for transitions from the ground state fairly well. However, for transitions from excited states one has to rely on theory. For the majority of the transitions only approximation formulae are available. These should provide data accurate to a factor better than two, some claiming the uncertainties to be as small as  $\sim 20\%$ . Similar restrictions are found for electron-impact ionization data, which however are less important in practice.

Our model atoms comprise levels with principal quantum number up to  $n \leq 50$ , and energies adopted from Moore (1993). All lines are included assuming Stark profiles for transitions between energy levels with  $n \leq 7$ , applying the theory of Griem (1960) as implemented by Auer & Mihalas (1972), and Doppler profiles for the remainder. Transition probabilities are calculated using a routine of Storey & Hummer (1991). Photoionization cross-sections and the free-free opacity are evaluated applying hydrogenic expressions (Mihalas 1978, p. 99 & p. 102) with Gaunt factors treated according to Wright (1978) (see Appendix B).

We have constructed model atoms using data for electron-impact excitation according to Mihalas, Heasley & Auer (1975, MHA), the approximation formulae of Johnson (1972, J72) and Percival & Richards (1978, PR) and the *ab-initio* calculations of Anderson et al. (2000; 2002, ABBS) and Butler (in preparation, B04) for transitions between lower/upper levels  $n, n'$ , see Table 1. A few of the collision rates are illustrated in Fig. 1. All the rates are in good agreement for the  $n=1-2$  transition since accurate data were available to Johnson and MHA in this case. The classical results of PR are only valid for  $n, n'$  greater or equal to 5. They are only included in this case for reference. On the other hand there is considerable disagreement for the  $n=1-3$  and  $n=5-6$  transitions although in the latter case the PR results are close to those of B04. Overall both the Johnson and MHA

data show equally large departures from the modern results. For the higher  $n$  values the agreement between PR and B04 is better but there are still differences. These may be due to inadequacies in either approach and the question as to which data are to be preferred for these high  $n$  transitions can only be answered by more extensive calculations. In addition, the numerical fits of Giovanardi, Natta & Palla (1987, GNP) have been applied to the collisional excitation rates in some test cases. Electron-impact ionization rates are evaluated according to Mihalas (1967) for  $n \leq 10$  and by use of the Seaton formula (1962) for  $n > 10$ . For test purposes the approximation formula of Johnson (1972) has also been implemented for collisional bound-free processes, without significant impact.

In the final step with SURFACE the hydrogen spectrum is synthesised adopting wavelengths from Wiese, Smith & Glennon (1966). Stark broadening of the Balmer and Paschen lines is accounted for by the use of the tables of Stehlé & Hutcheon (1999, SH). In the case of the Brackett and Pfund lines we apply the theory of Griem (1960) as implemented by Auer & Mihalas (1972).

### 2.3. Model complexity

In addition to the choice of the atomic data, the complexity of the model atom can also influence the model predictions. In order to investigate this effect, model atoms are constructed with 10 to 50 explicitly treated energy levels. The model atoms are identified by a label plus the number of levels in the following. Both departure coefficients and line source functions obey an asymptotic behaviour (see below), such that the tests help to identify the minimum requirements for model complexity.

A complication arises as a result of the interaction of the hydrogen atoms with the stellar plasma. High-lying energy levels are broadened as they are perturbed, and finally dissolved – the Stark broadening of the hydrogen lines near the series limits gives rise to a quasi-continuum. Our straightforward approach reproduces the observed series limit behaviour (highest-frequency series member with separately discernible profile, i.e. the classical Inglis-Teller limit, and the flux distribution throughout the line region and quasi-continuum) in the cases where the available spectra cover these regions. Despite this success, the solution is not fully self-consistent, and future work will incorporate the occupation probability formalism of Hubeny, Hummer & Lanz (1994) for improvement.

## 2.4. Discussion

The mechanisms driving departures of H I from detailed balance in stellar atmospheres have been well understood since the seminal work of Auer & Mihalas (1969a; 1969b, for early-type stars), and numerous subsequent contributions – for line formation in the IR e.g. by Zaal et al. (1999). We do not intend to repeat these arguments. We only wish to point out that the atomic data on radiative processes in H I are of high accuracy, thus excluding a source of systematic uncertainty compromising studies of most ions of the other elements. The issue here is the impact of the *local* processes that affect the radiatively induced departures from LTE, namely collisional interactions, which are assumed to be of secondary importance. Indeed, various choices of the (mostly approximate) data produce no significant differences in the stellar continuum or the Balmer line profiles, i.e. the features that are the starting point for quantitative analyses using model atmosphere techniques.

But consider Fig. 2, where we summarise the results from our model calculations for Br $\alpha$  and Pf $\alpha$  for atmospheric parameters that match those of Vega, one of the best-studied stars. Apparently, the choice of collisional data is not a second-order effect, but a dominant factor for line-formation computations in the IR. The only way to determine which data should be used is by comparison of the models with observation over all parameter space.

Before this is done in the following section, we wish to discuss the effects of the different atomic model implementations in more detail, in anticipation of the results to come. We choose our model for  $\beta$  Ori to illustrate this, as the non-LTE effects are amplified in a supergiant (although the rôle of collisions are somewhat diminished in such tenuous atmospheres), but the results are similar in the general stellar context. They also allow more general conclusions to be drawn, as the atomic data are valid – under normal circumstances – independent of environment.

Departure coefficients  $b_i = n_i/n_i^*$  (the  $n_i$  and  $n_i^*$  being the non-LTE and LTE populations of level  $i$ , respectively) for selected levels using models A30–F30 are displayed in Fig. 3. The overall behaviour, i.e. the over- and underpopulation of the levels of the minor ionic species and the major species H II, is governed by the radiative processes, while the differences in the collisional data lead to modulations. These are small for the ground state and become only slightly more pronounced for the  $n = 2$  level, as these are separated by comparatively large energy gaps from the remainder of the term structure. Only colliding particles in the high-velocity tail of the Maxwellian velocity-distribution are able to overcome these energy differences at the temperatures encountered in the star’s atmosphere. Thus, computations of the model atmosphere structure will not be significantly influenced, as the important bound-free opacities of hydrogen vary only slightly. Line-formation computations in the IR on the other hand will be affected, as maximum effects from variations of the collisional data

are found for the levels with intermediate  $n$  at line-formation depth. In fact, the differences in the collisional cross-sections from approximation formulae and *ab-initio* computations are largest for transitions among the  $n = 3-7$  levels with  $\Delta n = 1$  and 2, and they can amount to more than an order of magnitude. The higher Rydberg states again show less sensitivity as they approach the limiting case of LTE, which is independent of the details of individual (de-)populating mechanisms. Detailed collisional cross-sections from *ab-initio* computations up to  $n \simeq 7$  are therefore sufficient to eliminate a significant source of systematic error. However, using the available data it turns out that the MHA- (models A, C, E) and J72-type approximations (models B, D, F) give rise to basically two sets of distinct behaviour, with the former tending to dampen non-LTE departures more efficiently than the latter, due to larger collisional cross-sections. Such differences in the level populations are the cause for the line-profile variations. This is also evident in Fig. 4, where the response of the line-source function  $S_L$  to variations in the collisional data is displayed. Here, models A and F usually define both extremes. The IR lines experience a non-LTE strengthening in this star. Comparison with observed IR lines will be highly valuable in selecting the preferable collisional data. We remember that the line source function may be written as

$$S_l = \frac{2h\nu^3/c^2}{b_i/b_j \exp(h\nu/kT) - 1} \quad (1)$$

so that the source function is particularly sensitive to variations in the ratio of the departure coefficients

$$\begin{aligned} |\Delta S_l| &= \left| \frac{S_l}{b_i/b_j - \exp(-h\nu/kT)} \Delta(b_i/b_j) \right| \\ &\approx \left| \frac{S_l}{(b_i/b_j - 1) + h\nu/kT} \Delta(b_i/b_j) \right| \end{aligned} \quad (2)$$

when  $h\nu/kT$  is small. This makes these lines very susceptible to small changes in the atomic data and details of the calculation. Indeed, the emission cores of Br $\alpha$  and Pf $\alpha$  predicted by model A in Vega (Fig. 2) result from such a non-LTE amplification. For Pf $\alpha$  the  $\Delta(b_5/b_6)$  between model A and E amounts to only  $\lesssim 2\%$  at the line-core formation depth, with the  $b_5/b_6$  ratios for the different model atoms deviating even less from unity.

Note that because of our restricted approach (plane-parallel, hydrostatic atmosphere) this discussion is only realistic for the inner photosphere ( $\log \tau_{\text{ross}} \gtrsim -2$ ) in this supergiant, so that significant differences between the model predictions and observations for the first members of each series can be expected with regard to their line-formation depths. For H $\gamma$  this typically manifests itself in the line core where the observed profile is shallower than that predicted, while the line wings are reproduced. In the more luminous supergiants H $\alpha$  develops into a completely wind-dominated P-Cygni line. The modelling of the higher series

members on the other hand can be expected to be more accurate, as they are formed deeper in the photosphere.

As indicated in the last section, another issue is of concern, the complexity of the model atom, if level dissolution is not explicitly accounted for. Level populations may vary with the number of explicitly treated states, as more channels for the (de-)population of individual levels are opened. The results from test calculations for our model of  $\beta$  Ori are shown in Figs. 5 and 6. An obvious feature is the convergent behaviour of departure coefficients and line source functions with increasing number of levels. Both asymptotically approach values set by models of considerable complexity. In the case of this star a  $\sim 25$ – $30$ -level model atom is required to achieve this at depths relevant to line formation. This coincides with the classical Inglis-Teller limit. More simplistic model atoms turn out to overestimate the  $n = 3$ – $5$  populations at line-formation depths in particular, with the effect becoming smaller for higher  $n$ . Comparison with observations of Paschen, Brackett and Pfund lines is therefore most promising in order to verify this finding empirically. Increasing the number of explicitly treated levels even further has only an impact in the outermost layers, which are not properly computed for supergiants in our approach. Moreover, these high-lying Rydberg states will be subject to level dissolution in a real plasma. However, such complex model atoms are instructive as they nicely demonstrate how the departure coefficients of the higher H I Rydberg states approach the limit set by H II, see Fig. 5 (lower right panel), due to tight collisional coupling i.e. the limiting case of LTE.

Despite being instructive in their own, the previous considerations can only provide indirect evidence for the choice an optimum model atom. A real selection can only happen via confrontation with observation, as approximations still have to be relied upon to a certain degree. This is done in the following on the basis of high-quality spectra for a few well-studied objects, in order to minimise the impact of other systematic error, such as uncertain stellar parameters.

### 3. Confrontation with observation

#### 3.1. The spectra

This work has to rely on a variety of sources for the observations. Some of the spectra in the visual and near-IR have been investigated in our earlier publications. The Vega (HD172167) spectrum was obtained using FOCES on the Calar Alto 2.2m telescope, and the  $\eta$  Leo (HD87737) and  $\beta$  Ori (HD34085) spectra were acquired with FEROS on the ESO 1.5m telescope at La Silla. Both instruments are Echelle spectrographs, and the data were ob-

tained at a resolving power of  $R = \lambda/\Delta\lambda \sim 40000$  and  $48000$ , respectively. More detailed information on the observations and data processing can be found in Przybilla et al. (2001) and Przybilla & Butler (2001). Medium-resolution ( $R \sim 3000$ ) IR spectra in the  $J$ ,  $H$  and  $K$  band for Vega and  $\eta$  Leo are adopted from the catalogues of Wallace et al. (2000), Meyer et al. (1998) and Wallace & Hinkle (1997), see these for details. We have rectified these KPNO 4m/FTS spectra for our purposes. Similar data for  $\beta$  Ori have been kindly provided by A. Fullerton (private communication), obtained with CFHT/FTS at  $R \sim 10000$ , see Fullerton & Najarro (1998) for details.

The blue visual spectrum for  $\tau$  Sco (HD149438) is adopted from the work of Kilian & Nissen (1989), who used the CASPEC spectrograph on the ESO 3.6m telescope ( $R \sim 20$ – $25000$ ). Both, the  $H\alpha$  and the IR spectra for this object were kindly provided by P.A. Zaal. The MUSICOS spectrograph on the INT at La Palma was used to obtain the former ( $R \sim 30000$ ) and UKIRT/CGS4 for the latter ( $R \sim 14$ – $16000$ ), see Zaal et al. (1999) for details on the observations and data reduction. Optical spectra of HD 93250 as observed with ESO NTT/EMMI ( $R \sim 5$ – $6000$ ) are adopted from Puls et al. (1996), while the  $K$  band data (CTIO 4m/OSIRIS,  $R \sim 1100$ ) for this star are taken from the  $2\mu$  atlas of hot, luminous stars by Hanson, Conti & Rieke (1996). See these publications for additional information on the observations and data reduction procedures.

For the comparison of the synthetic with observed spectra, the former are convolved with a Gaussian of full width at half-maximum appropriate to the instrumental resolution in all cases where this is a non-negligible factor. All observed spectra are radial velocity corrected to the rest frame via cross-correlation with appropriate synthetic spectra.

### 3.2. Atmospheric parameters

The stellar parameters adopted for model calculations for the objects discussed here are summarised in Table 2: spectral type, effective temperature  $T_{\text{eff}}$ , (logarithmic) surface gravity  $\log g$ , helium abundance (by number)  $y$ , stellar radius  $R$ , (logarithmic) stellar luminosity  $\log L$ , (micro-)turbulent velocity  $v_t$  and projected rotational velocity  $v \sin i$ . Additional data are provided where necessary for calculations with FASTWIND: mass-loss rate  $\dot{M}$ , wind terminal velocity  $v_\infty$  and wind velocity parameter  $\beta$ . All data have been determined from spectroscopic indicators using standard techniques, the fundamental atmospheric parameters surface gravity and effective temperature e.g. from fitting the Balmer line wings and several non-LTE ionization equilibria: He I/II and/or Si III/IV for the objects with  $T_{\text{eff}} \geq 30000$  K, and N I/II and Mg I/II for the cooler objects – HD 93250: Repolust, Puls & Herrero (2003);  $\tau$  Sco: Kilian et al. (1991);  $\eta$  Leo and  $\beta$  Ori: Przybilla & Butler (2001), Przybilla et al. (2001).



### 3.3. Line profile fits

We begin our investigations with Vega, one of the most-intensely studied stars, and in most respects well described by the assumption of LTE. The Balmer and Paschen lines are in general well matched by LTE computations, and these are practically identical to the non-LTE results. However, comparison with the observed Br $\gamma$  profile in Fig. 7 shows that LTE modelling fails to reproduce the line core correctly. Non-LTE computations can improve on this, except for model A, which differs only slightly from LTE. However, on the basis of this one case alone a decision as to which model atom should be favoured cannot be drawn, as despite being noticeable the differences between models B to F are not highly significant. Moreover, the model complexity will also affect the line-formation computations as shown in Fig. 8. In this case the 10-level model atoms would predict too shallow a line core, close to the LTE result, and the 25- and 30-level models a line core that is too deep. Note that this sensitivity distinguishes model atoms using the J72 approximation from those applying the MHA approximation, which are far less affected.

Additional observations of Br $\alpha$  and Pf $\gamma$  in the *L*-band are available (Wallace & Hinkle 2002). However the lower S/N of the data restricts their usefulness for our purposes, except for ruling out LTE modelling and model atom A. Additional complications arise in the case of Br $\alpha$ , where the computations predict a significantly too deep line core for models B–F. This may be an indication of neglected non-LTE effects on the atmospheric structure, as the line core is formed at atmospheric layers unsampled by the higher series members. A similar effect is found in the very line core of H $\alpha$  (here the models indicate a too shallow line), which is formed at similar atmospheric depths.

Non-LTE effects get strengthened in supergiants, and we can expect differences in the predictions from different model atoms to become amplified in the same way. Indeed, comparison of theoretical line profiles with observations for the two bright BA-type supergiants  $\eta$  Leo and  $\beta$  Ori in Fig. 9 shows marked differences, and allows us to make an important step in constraining an optimum model atom. H $\gamma$  in both supergiants is again barely affected by details of the model atoms, and the deviations from LTE are small. However, stellar wind emission may fill the line cores and consequently in such a case a good profile fit can only be obtained for the wings in our approach. This also affects P $\gamma$  and Br $\gamma$ , but we can definitely rule out LTE line formation as a means of reproducing the observations, as the predicted lines are too weak, and the model atoms employing the J72 approximation (profiles from models B and D resemble the model F predictions and are not shown here) appear to produce lines that are significantly too strong. Note that the discrepancies with P $\gamma$  in  $\eta$  Leo may be related to the lower S/N of the spectral data. These conclusions are confirmed by modelling of the higher Brackett lines in the *H*-band, which are expected to be unaffected

by the stellar wind, see Fig. 10. Model E gives an excellent fit, improving slightly on model C, but all other models fail to reproduce the observations.

An analogous situation is found for the lines of the Paschen series in supergiants, which show similar sensitivity to electron collision data as the Brackett series members. This is in contrast to main sequence stars like Vega, where deviations from LTE are negligible for the Paschen series, see Fig. 11. Note the high quality of the synthesis of the series limits and the transition into the continuum, despite having not incorporated an occupation probability formalism into the modelling. This also applies to the Balmer series.

Non-LTE effects also strengthen with increasing temperature, and despite the increasing dominance of radiative transitions over collision processes some interesting conclusions can be drawn. In the following we will concentrate on the main sequence, where higher atmospheric densities lead to stronger effects of modified collision cross-sections, and lower luminosities than in supergiants reduce the effects of the stellar wind on the line formation. Two stars are selected: the well-studied object  $\tau$  Sco (B0 V) and the most luminous main sequence object of the sample of Repolust et al. (2003), HD 93250, of spectral type O3 V ((f)).

The results from our hydrostatic and plane-parallel modelling for selected hydrogen lines of  $\tau$  Sco are displayed in Fig. 12. Detailed collision data improves the spectrum synthesis in the very line cores of  $H\beta$  and  $H\gamma$ , but for  $H\alpha$  and the IR-lines a good match cannot be obtained. Intriguingly, model A provides a reasonable fit to the IR emission profiles. We reproduce the findings of Zaal et al. (1999), see their Figs. 13 and 14, *using a line-blanketed LTE model atmosphere*. In view of this and our previous discussion we may conclude that the emission does not occur because of a temperature inversion in the outer layers of the atmosphere, which is absent in our LTE model atmosphere. The IR emission predicted by model A is an artifact of the choice of the collisional atomic data, which leads to population inversion (see below).

The presence of a circumstellar disc around  $\tau$  Sco may offer an alternative explanation. Assuming the star to be a fast rotator seen pole-on, a low-density disk may show emission features in the IR hydrogen lines without revealing itself via  $H\alpha$ -emission (Zaal, Waters & Marlborough 1995). However, subsequent work by Zaal et al. (1997) finds single-peaked IR emission features on top of broad absorption lines being common among slow rotators rather than an exception, and they conclude that they are an atmospheric phenomenon. This leads to suggesting non-LTE population inversion as the source of the emission features, facilitated by the distinctive environment of a spherical and expanding atmosphere.

A comparison of our spectrum synthesis using a hydrodynamic approach with observation is made in Fig. 13. Note that the observations were obtained during four epochs

spanning  $\sim 10$  years, so that a single set of stellar parameters may be insufficient to reproduce all lines simultaneously, given an observed variability of the Br $\alpha$  equivalent width (Zaal et al. 1999). The overall agreement is nonetheless good, with the exception of Br $\alpha$ , if one allows for a slight adjustment of the stellar wind parameter  $\beta$  (note that  $\beta \simeq 2.5$  implies a shallower velocity law than that typical of OB-type stars from UV/optical studies, where  $\beta \simeq 0.8$ ). We have to stress again that even small variations of the level departures can drastically affect the line source function in the IR (Eqn. 2) when being close to population inversion, which turns out to be the case for  $\tau$  Sco. In order to produce an excellent fit sound modelling is required, demanding not only *perfect* atomic data but also knowledge of the *exact* atmospheric conditions at line-formation depth. Several factors are limiting the accuracy at present, most important among those the approximative treatment of the temperature structure and the details of connecting the (pseudo)-hydrostatic photosphere and the stellar wind, as the (emission) line cores are formed in the transition region. These prohibit any further conclusions on the accuracy of the atomic data beyond those already drawn.

Nonetheless, two additional tests have been performed for improving the modelling of Br $\alpha$ , in particular to account for the absence of absorption wings in the observations, and in order to match the width (and height) of the emission peak. Incoherent electron scattering offers one possibility to fill the absorption wings, via the frequency redistribution of photons from the emission peak by an electron layer of sufficient optical depth. However, little improvement is achieved by accounting for this effect, as the stellar wind is too thin. Clumping of the stellar wind also has the potential to affect line strengths. The presence of clumping in the wind of  $\tau$  Sco has been proposed by Howk et al. (2000) in order to explain some peculiar far-UV features and the extremely hard X-ray emission observed in this star. In general, it is also supported by a number of UV-analyses. Based on FUSE-observations of Magellanic Cloud stars, Crowther et al. (2002), Massa et al. (2003) and Hillier et al. (2003) found indications of wind clumping. Additional support is given by the analysis of optical data, displaying a systematic difference of observed and theoretically predicted wind-momentum rates for supergiants (Puls et al. 2003; Repolust et al. 2003). Test computations for an increased mass-loss rate can reproduce the absence of wings and the width of Br $\alpha$ , however without properly matching the height of the emission peak simultaneously. The  $\dot{M}$  required for achieving this is approximately an order of magnitude higher than the present value, bringing the predictions for the other hydrogen lines into disagreement with observation. We thus cannot rule out clumping effects in the case of  $\tau$  Sco, however a more sophisticated approach should be investigated separately, as this goes beyond the scope of the present study.

Finally, HD 93250 may act as a benchmark for the study of objects at the earliest phases of stellar evolution of massive stars. Typically, the very young objects are deeply embedded

in a (ultra)-compact H II-region prohibiting spectroscopy in the visual. In order to study the immediate outcome of the star-formation process, stellar parameters have to be determined from the IR features. We conclude from Fig. 14 that simultaneous agreement between the modelling in the visual and in the  $K$ -band is achieved if detailed electron collision data is accounted for (as in model E). Here, radiative transitions dominate over collisions, such that most of the model profiles coincide. The only noticeable differences occur for model A, where the predicted equivalent widths are smaller by  $\sim 15\%$ . Computations using model atom X have been performed in this case only. In addition to the inconsistencies in the GNP dataset from theoretical considerations, as reported by Chang, Avrett & Loeser (1991), the computations indicate a significantly poorer fit than achieved using model atoms A (Fig. 14). Consequently, these data should be avoided in quantitative non-LTE modelling of the hydrogen IR lines.

#### 4. Recommendations

In view of the comparison of the predictions of different model atoms for H I with observation we can conclude that the use of electron collision data from *ab-initio* computations is *mandatory* in order to derive consistent results for the visual and IR. Model atoms relying on the MHA and J72 approximation data obviously fail in achieving this over the entire range of OBA-type stars. Introduction of detailed collision data such as those of ABBS or B04 largely remove the discrepancies. However, slight differences in the atomic data in combination with the use of approximation data for transitions involving levels with high  $n$ , which cannot be entirely abandoned in the modelling, still result in a variety of distinguishable predictions. Among the model atoms implemented, model E provides the best overall agreement between observation and the spectrum synthesis over the whole parameter space investigated here. Consequently, we recommend the data of B04 for the evaluation of collision rates of H I, supplemented by the approximation formulae by PR and of MHA for those transitions not covered by the *ab-initio* computations. This applies not only to the modelling of massive stars as we have done but to all hydrogen plasmas.

With regard to the model complexity for the non-LTE computations we suggest the use of a model atom with a number of explicitly treated levels according to the classical Inglis-Teller limit for a given star, when not accounting for the occupation probability formalism as implemented by Hubeny et al. (1994). Use of the atomic data recommended above further helps to minimise artifacts introduced by a model atom of inappropriate complexity.

We are grateful to J. Puls for providing the FASTWIND code and valuable comments

on the manuscript, and to F. Najarro and R.P. Kudritzki for helpful discussion. This work benefited much from the kind provision of spectra by A. Fullerton, K. Hinkle and P.A. Zaal. The NSO/Kitt Peak FTS data used here were produced by NSF/NOAO.

### A. Electron-impact excitation data

Here we summarise some results of the *ab-initio* computations of Butler (2004, in preparation) for electron-impact excitation cross-sections in hydrogen relevant for the present work. The *R*-matrix method in the close-coupling approximation was used to obtain data for hydrogen for all transitions between states with principal quantum number  $n \leq 7$  and angular momentum quantum number  $\ell \leq 6$ . For practical applications thermally-averaged effective collision strengths between lower and upper states  $i$  and  $j$  may be defined

$$\Upsilon_{ij} = \int_0^\infty \Omega_{ij} \exp(E_j/kT) d(E_j/kT) \quad (\text{A1})$$

where  $\Omega_{ij}$  is the collision strength and  $E_j$  the kinetic energy of the outgoing electron. The excitation rate coefficient is then

$$q_{ij} = \frac{8.63 \times 10^{-6}}{g_i T^{1/2}} \Upsilon_{ij} \exp(\Delta E_{ij}/kT) \text{ cm}^3 \text{ s}^{-1} \quad (\text{A2})$$

where  $g_i$  is the statistical weight of state  $i$  and  $\Delta E_{ij}$  the energy difference between the two states. The effective collision strength is dimensionless and symmetric, i.e.  $\Upsilon_{ij} = \Upsilon_{ji}$ .

Data for transitions between levels  $n$  and  $n'$ , i.e. summarised over the degenerate states with different quantum number  $\ell$ , are given in Table 3 for a wide range of temperatures. Details on the computations and the entire dataset will be discussed by Butler (2004, in preparation).

### B. Gaunt factors

The gaunt factors that we use (Wright, 1978) have not been published so we give the relevant data here. The fits have the form

$$\begin{aligned} g_{\text{II}} &= a_1 + \frac{b_1}{\nu} + \frac{c_1}{\nu^2} & 10^{16} \text{ s}^{-1} > \nu > \frac{3.28805 \times 10^{15}}{n^2} \text{ s}^{-1} \\ g_{\text{II}} &= a_2 + \frac{b_2}{\nu} + \frac{c_2}{\nu^2} & 6 \times 10^{16} \text{ s}^{-1} > \nu > 10^{16} \text{ s}^{-1} \end{aligned}$$

and the coefficients are to be found in Table 4. The uncertainties of the fits are typically less than 0.3%.

## REFERENCES

- Anderson, H., Ballance, C. P., Badnell, N. R., & Summers, H. 2000, *J. Phys. B*, 33, 1255 (ABBS)
- Anderson, H., Ballance, C. P., Badnell, N. R., & Summers, H. 2002, *J. Phys. B*, 35, 1613 (ABBS)
- Auer, L. H., & Mihalas, D. 1969a, *ApJ*, 156, 157
- Auer, L. H., & Mihalas, D. 1969b, *ApJ*, 156, 681
- Auer, L. H., & Mihalas, D. 1972, *ApJS*, 24, 193
- Butler K., & Giddings J. 1985, *Newsletter on Analysis of Astronomical Spectra No. 9*, University of London
- Chang, E. S., Avrett, E. H., & Loeser, R. 1991, *A&A*, 247, 580
- Crowther, P. A., Hillier, D. J., Evans, C. J., Fullerton, A. W., De Marco, O., & Willis, A. J. 2002, *ApJ*, 579, 774
- Fullerton, A. W., & Najarro, F. 1998, in *Boulder-Munich II: Properties of Hot, Luminous Stars*, ASP Conf. Ser. Vol. 131, ed. I. D. Howarth (San Francisco: ASP), 47
- Giddings J. R. 1981, Ph.D. Thesis, University of London
- Giovanardi, C., Natta, A., & Palla, F. 1987, *A&AS*, 70, 269 (GNP)
- Griem, H. R. 1960, *ApJ*, 132, 883
- Hanson, M. M., Conti, P. S., & Rieke, M.J. 1996, *ApJS*, 107, 281
- Hillier, D. J., Lanz, T., Heap, S. R., Hubeny, I., Smith, L. J., Evans, C. J., Lennon, D. J., & Bouret, J. C. 2003, *ApJ*, 588, 1039
- Howk, J. C., Cassinelli, J. P., Bjorkman, J. E., & Lamers, H. J. G. L. M. 2000, *ApJ*, 534, 348
- Hubeny, I., Hummer, D. G., & Lanz, T. 1994, *A&A*, 282, 151
- Johnson, L. C. 1972, *ApJ*, 174, 227 (J72)
- Kilian, J., & Nissen, P. E. 1989, *A&A*, 80, 255

- Kilian, J., Becker, S.R., Gehren, T., & Nissen, P. E. 1991, *A&A*, 244, 419
- Kurucz, R. L. 1993, Kurucz CD-ROM No. 13, Smithsonian Astrophysical Observatory, Cambridge, Mass.
- Massa, D., Fullerton, A. W., Sonneborn, G., & Hutchings, J. B. 2003, *ApJ*, 586, 996
- Meyer, M. R., Edwards, S., Hinkle, K. H., & Strom, S.E. 1998, *ApJ*, 508, 397
- Mihalas, D. 1967, *ApJ*, 149, 169
- Mihalas, D., Heasley, J. N., & Auer, L. H. 1975, A Non-LTE Model Stellar Atmospheres Computer Program, NCAR-TN/STR 104 (MHA)
- Mihalas, D. 1978, *Stellar Atmospheres*, 2nd edition (Freeman, San Francisco)
- Moore, C.E. 1993, in *Tables of spectra of hydrogen, carbon, nitrogen, and oxygen atoms and ions*, ed. J.W. Gallagher (CRC Press, Boca Raton)
- Percival, I. C., & Richards, D. 1978, *MNRAS*, 183, 329 (PR)
- Przybilla, N., & Butler, K. 2001, *A&A*, 379, 955
- Przybilla, N., Butler, K., Becker, S. R., & Kudritzki, R. P. 2001b, *A&A*, 369, 1009
- Puls J., et al. 1996, *A&A*, 305, 171
- Puls, J., Repolust, T., Hoffmann, T., Jokuthy, A., & Venero, R. 2003, in *A Massive Star Odyssey, from Main Sequence to Supernova*, Proc. IAU Symp. No. 212, ed. K. A. van der Hucht, A. Herrero, & C. Esteban (San Francisco: ASP), 61
- Repolust, T., Puls, J., & Herrero, A. 2003, *A&A*, in press
- Rybicki, G. B., & Hummer, D. G. 1991, *A&A*, 245, 171
- Santolaya-Rey, A. E., Puls, J., & Herrero, A. 1997, *A&A*, 323, 488
- Seaton, M. J. 1962, in: *Atomic and Molecular Processes* (Academic Press, New York)
- Stehlé, C., & Hutcheon, R. 1999, *A&AS*, 140, 93 (SH)
- Storey, P. J. & Hummer, D. G. 1991, *Comput. Phys. Commun.*, 66, 129
- Wallace, L., Hinkle, K. 1997, *ApJS*, 111, 445
- Wallace, L., Meyer, M. R., Hinkle, K., & Edwards, S. 2000, *ApJ*, 535, 325

Wallace, L., Hinkle, K. 2002, *AJ*, 124, 3393

Wiese, W. L., Smith, M. W., & Glennon, B. M. 1966, *Atomic Transition Probabilities, Vol. I*, NSRDS-NBS 4 (NBS, Washington, D.C.)

Wright, S.L. 1978, Ph.D. Thesis, University of London

Zaal, P. A., Waters, L. B. F. M., & Marlborough, J. M. 1995, *A&A*, 299, 574

Zaal, P. A., Waters, L. B. F. M., Geballe, T. R., & Marlborough, J. M. 1997, *A&A*, 326, 237

Zaal, P. A., de Koter, A., Waters, L. B. F. M., Marlborough, J. M., Geballe, T. R., Oliveira, J. M., & Foing, B.H. 1999, *A&A*, 349, 573



Table 1. Non-LTE Model Atoms

Model	Electron-impact excitation data
A	MHA (all $n, n'$ )
B	J72 (all $n, n'$ )
C	ABBS ( $n, n' \leq 5$ ), MHA (rest)
D	ABBS ( $n, n' \leq 5$ ), J72 (rest)
E	B04 ( $n, n' \leq 7$ ), PR ( $n, n' \geq 5$ ), MHA (rest)
F	B04 ( $n, n' \leq 7$ ), PR ( $n, n' \geq 5$ ), J72 (rest)
X	GNP ( $n, n' \leq 15$ ), MHA (rest)

Note. — see text for references

Table 2. Stellar Parameters

Object	Sp. Type	$T_{\text{eff}}$ (K)	$\log g$ (cgs)	$y$	$R/R_{\odot}$	$\log L/L_{\odot}$	$v_t$ (km s $^{-1}$ )	$v \sin i$ (km s $^{-1}$ )	$\dot{M}$ ( $10^{-6} M_{\odot} \text{ yr}^{-1}$ )	$v_{\infty}$ (km s $^{-1}$ )	$\beta$
Vega	A0 V	9550	3.95	0.09	2.8	1.78	2	22	...	...	...
$\tau$ Sco	B0 V	31400	4.24	0.09	5.1	4.36	3	19	0.009	2000	2.4/2.5
HD93250	O3.5 V	46000	3.95	0.09	15.9	6.01	0	130	3.45	3250	0.9
$\eta$ Leo	A0 Ib	9600	2.00	0.13	50	4.28	4	9	...	...	...
$\beta$ Ori	B8 Ia	12000	1.75	0.135	104	5.30	7	36	...	...	...

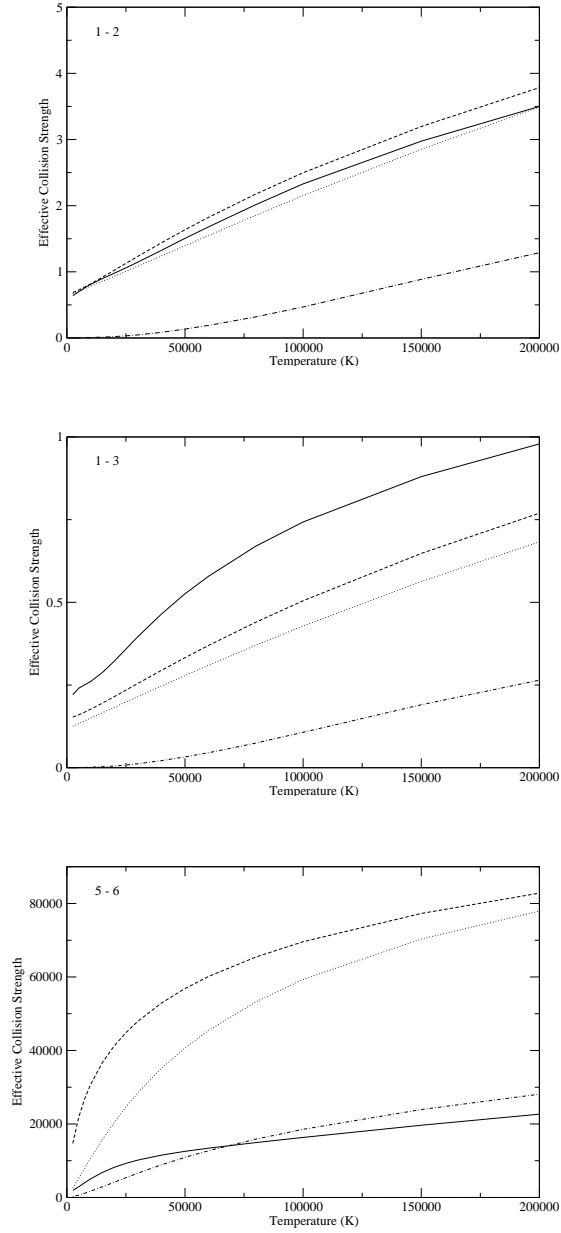


Fig. 1.— Comparison of effective collision strengths for several transitions  $n - n'$ , as indicated. The curves are: B04 (*solid*), J72 (*dotted*), MHA (*dashed*), PR (*dash-dotted*).

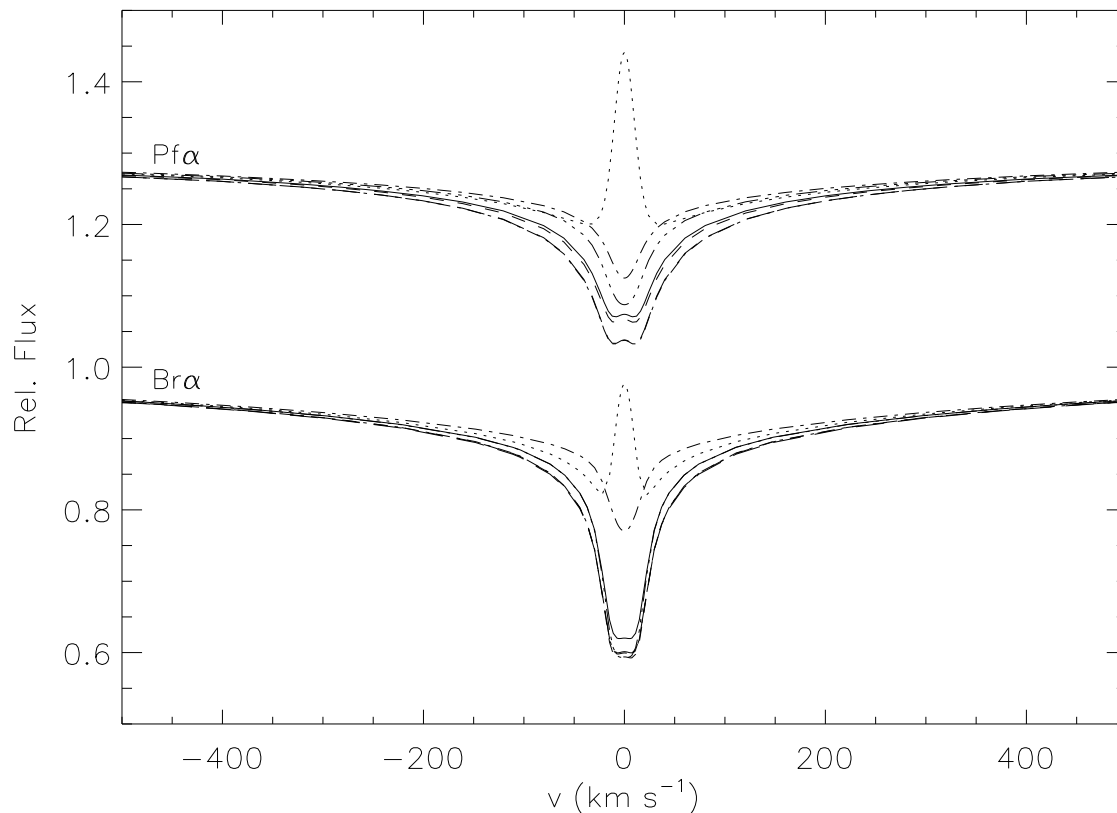


Fig. 2.— Comparison of model profiles for  $\text{Br}\alpha$  and  $\text{Pf}\alpha$  in Vega: models A, C, E, F (*dotted, dash-dot-dot-dotted, full, dashed lines*) and LTE (*dashed-dotted*). Models B, C and D are not resolved in the case of  $\text{Br}\alpha$  as they practically coincide with model F, forming the lowest set of graphs, as do models B and D in the case of  $\text{Pf}\alpha$ . The non-LTE computations are for a 20-level model atom. Abscissa is Doppler velocity relative to line centre. For clarity the different spectra are shifted by 0.3 units in ordinate.

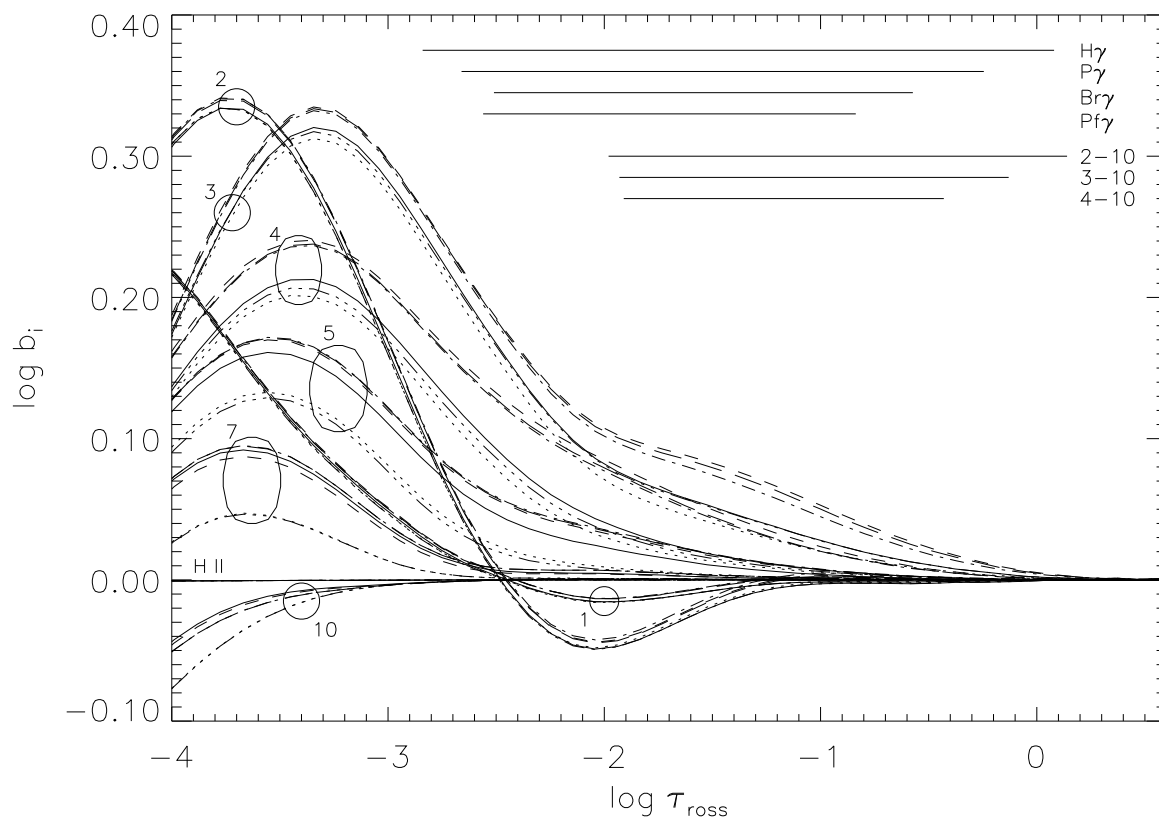


Fig. 3.— Run of departure coefficients  $b_i$  in  $\beta$  Ori as a function of Rosseland optical depth  $\tau_{\text{ross}}$ , models A–F (*dotted, dashed-dotted, dash-dot-dot-dotted, long dashed, full, dashed lines*). All non-LTE computations are for a 30-level model atom. The individual sets of graphs are labelled according to the level’s principal quantum number; all graphs for H II coincide. Line-formation depths for a few features are indicated.

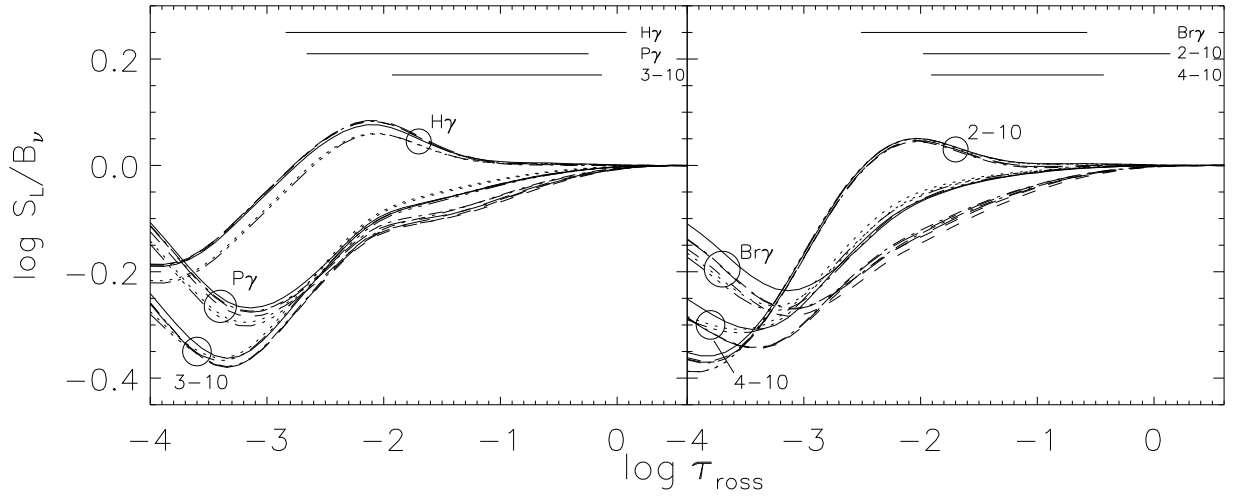


Fig. 4.— Ratio of line source function  $S_L$  to Planck function  $B_\nu$  at line centre as a function of  $\tau_{\text{ross}}$  in  $\beta$  Ori. Line designations as in Fig. 3.

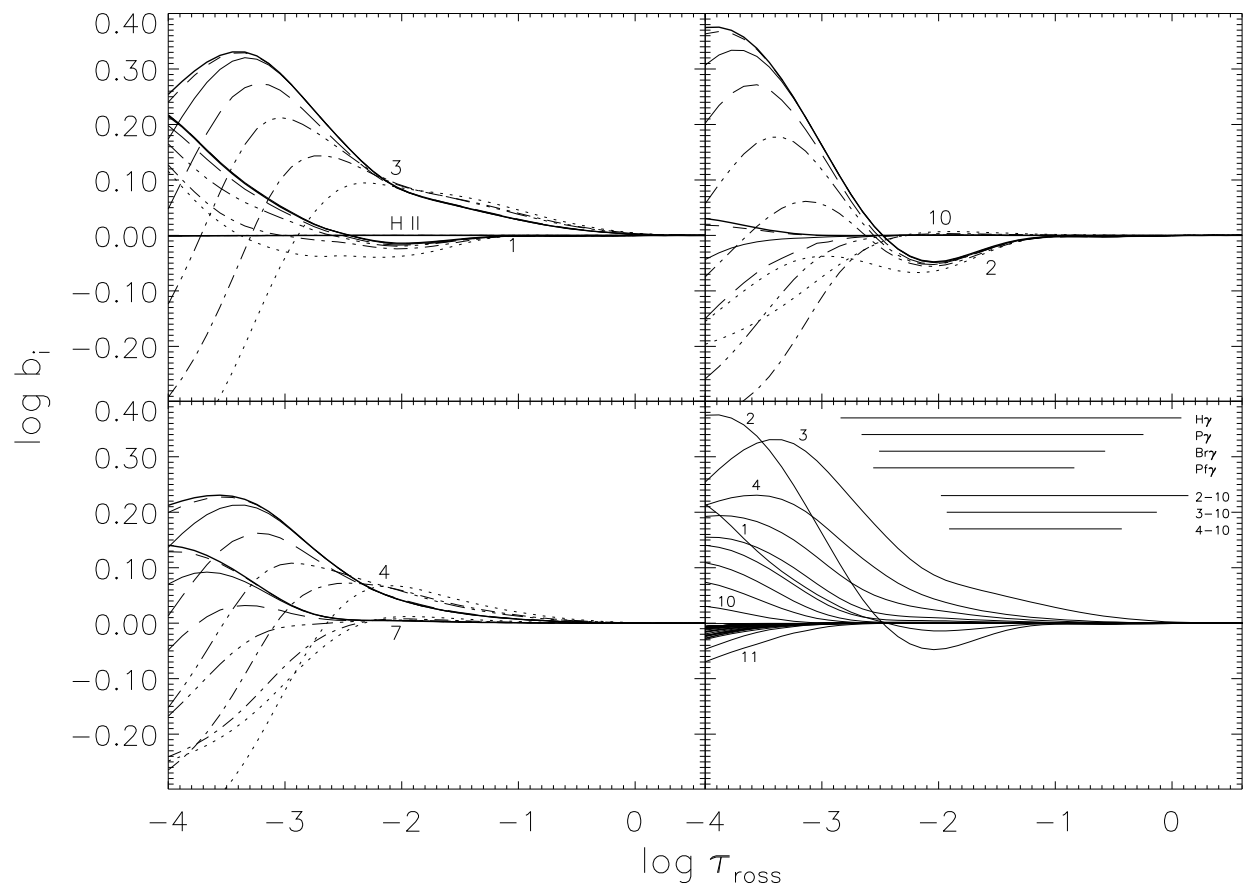


Fig. 5.— Run of  $b_i$  in  $\beta$  Ori as a function of  $\tau_{\text{ross}}$  for models E of different complexity: a 10, 15, 20, 25, 30, 40, 50-level model (*dotted, dashed-dotted, dash-dot-dot-dotted, long dashed, full, dashed, full thick lines*). The lower right panel displays the behaviour of all model E50 levels. Note the Rydberg states asymptotically approaching the H II limit.

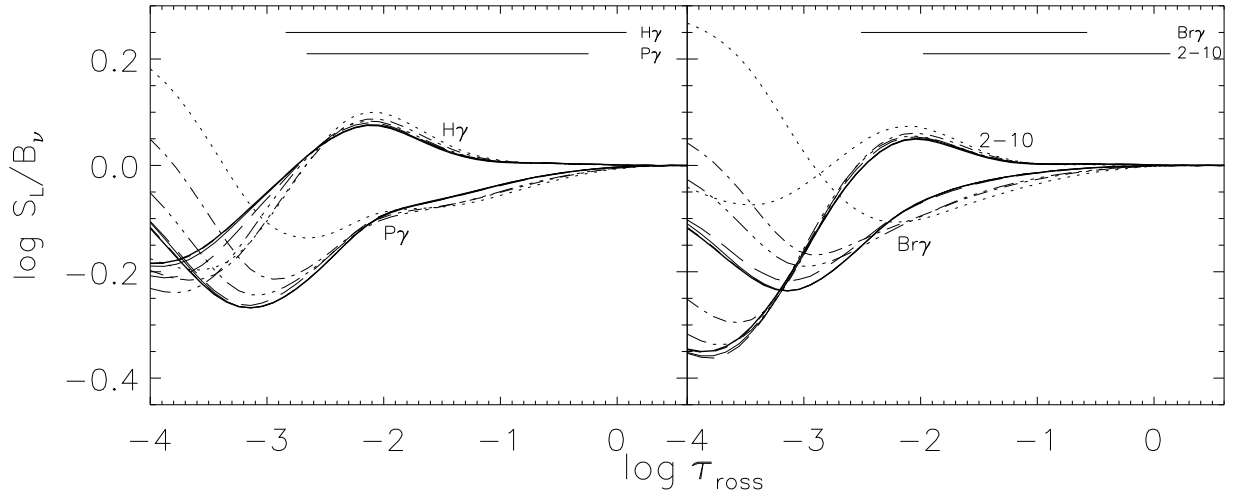


Fig. 6.— As Fig. 4, but for models E of different complexity (10–50 levels). Line designations as in Fig. 5.



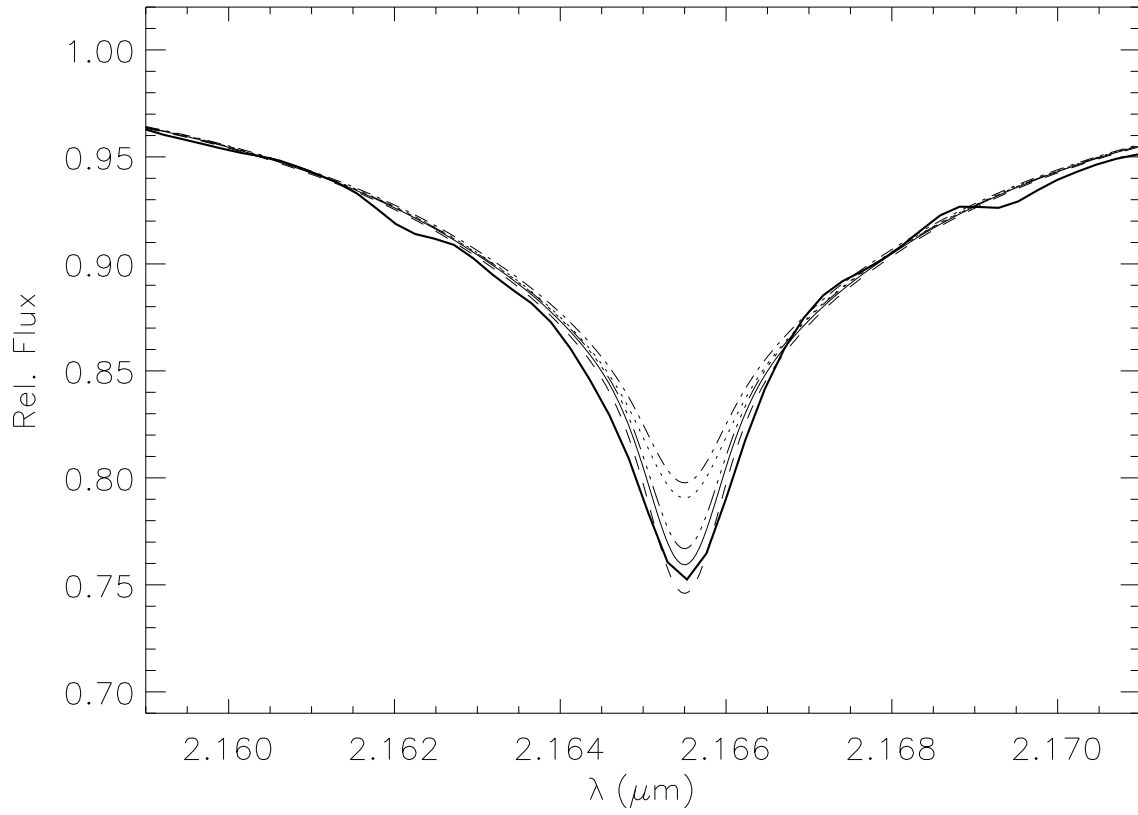


Fig. 7.— Spectrum synthesis for Br $\gamma$  in Vega: models A, C, E and F (*dotted, dash-dot-dotted, full, dashed lines*) and an LTE profile (*dashed-dotted*) are compared with observation (*thick full line*). Models B and D are omitted for clarity as they are almost identical to model F. All non-LTE computations are for a 20-level model atom.

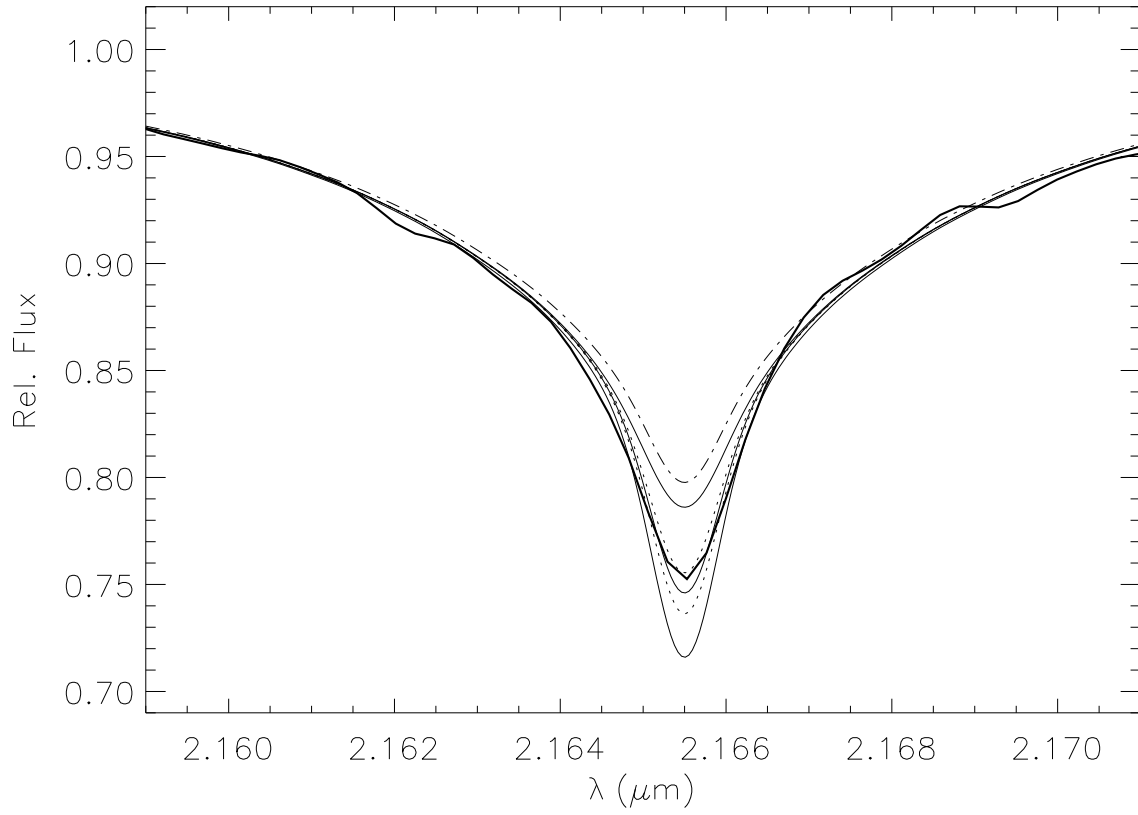


Fig. 8.— Like Fig. 7, for a 10, 15, 20, 25 and 30-level model F (*full and dotted lines in alteration, top to bottom*) and LTE (*dashed-dotted*).

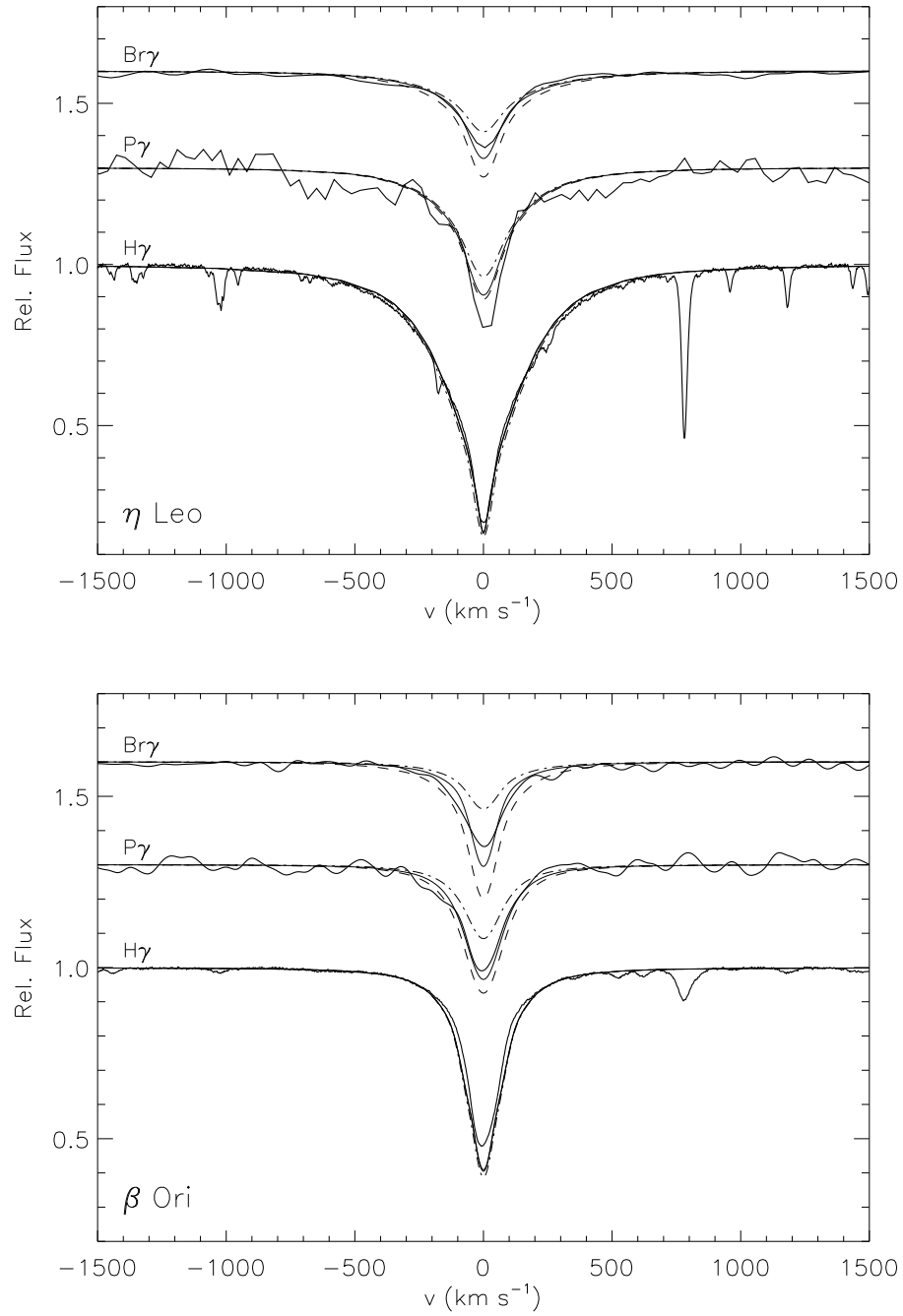


Fig. 9.—  $\text{H}\gamma$ ,  $\text{P}\gamma$  and  $\text{Br}\gamma$  in  $\eta$  Leo and  $\beta$  Ori, as indicated: models E30 (*full lines*), F30 (*dashed*) and LTE calculations (*dashed-dotted*) are compared with observation (*thick full lines*). For clarity the different spectra are shifted by 0.3 units in ordinate. Note the lower S/N of the  $\text{P}\gamma$  observations of  $\eta$  Leo.

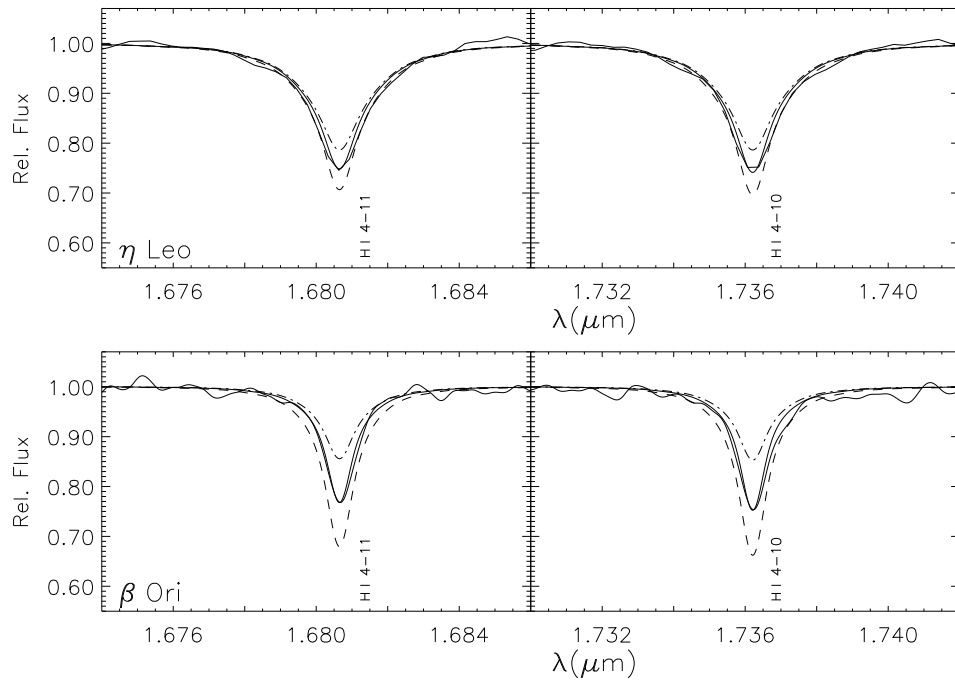


Fig. 10.— Higher Brackett lines in  $\eta$  Leo and  $\beta$  Ori, as indicated: models E30 (*full lines*), F30 (*dashed*) and LTE calculations (*dashed-dotted*) are compared with observation (*thick full lines*).

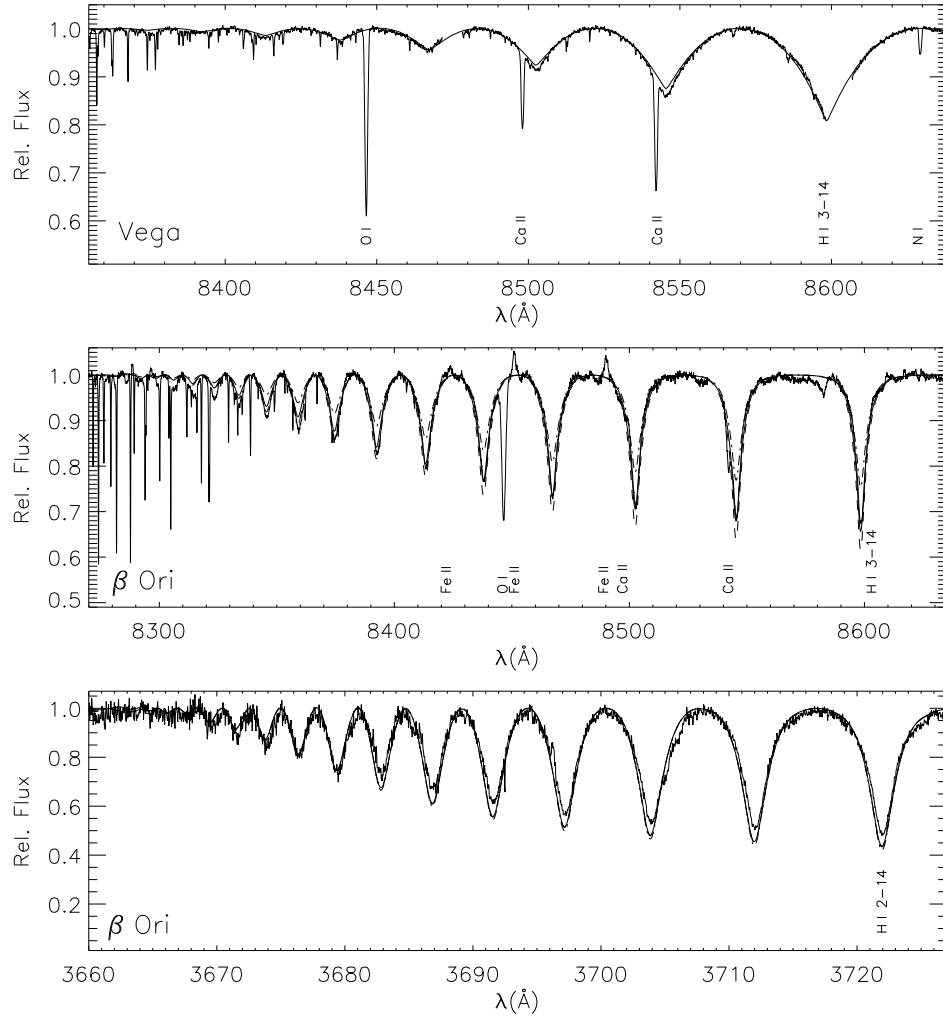


Fig. 11.— Series limits in Vega and  $\beta$  Ori, as indicated. Models E20 (*full line*, top), E30 and F30 (*full line* and *dashed*, lower two panels) and LTE profiles (*dashed-dotted*) are compared with observation (*thick full line*). Note the presence of a few gaps in the observed spectra, and numerous sharp telluric features.

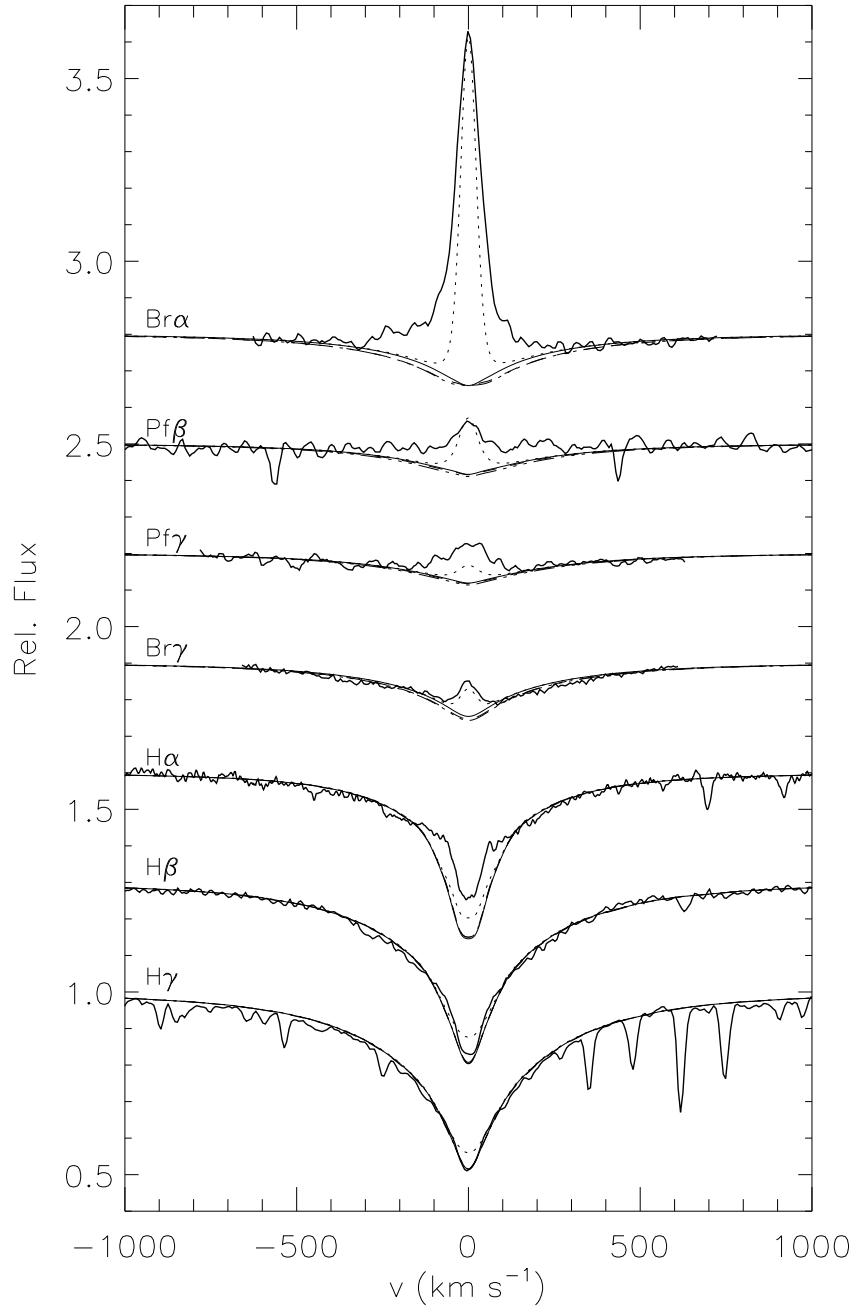


Fig. 12.— Spectrum synthesis for  $\tau$  Sco – hydrostatic/plane-parallel modelling: models A, B, E and F (*dotted*, *dash-dot-dot-dotted*, *full* and *dashed lines*) and observation (*thick full line*). All computations are made using a 15-level model atom. For clearness the different spectra are shifted by 0.3 units in ordinate.

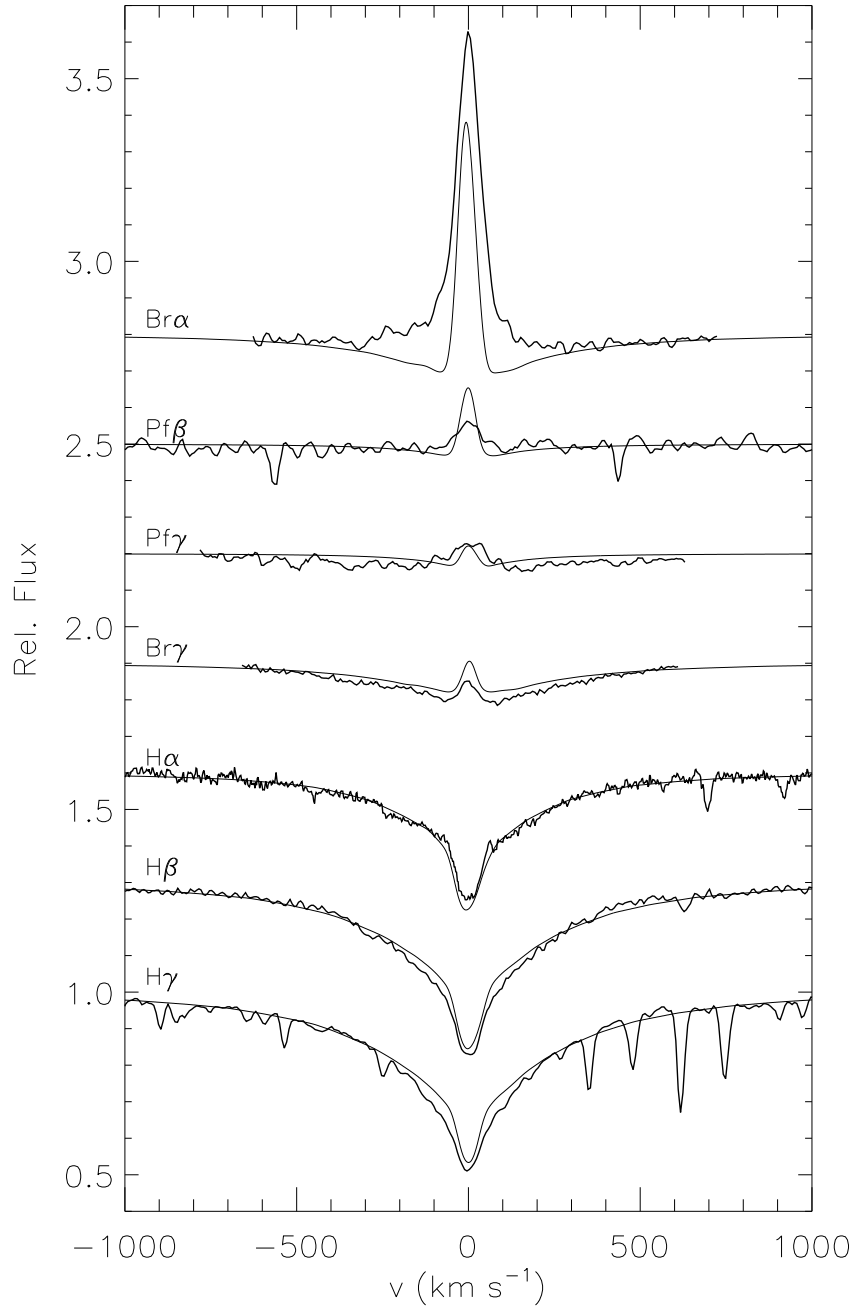


Fig. 13.— Spectrum synthesis for  $\tau$  Sco – hydrodynamic/spherical modelling: model E15 (*full line*) and observation (*thick full line*). A velocity field with  $\beta = 2.4$  is adopted, except for the modelling of the Brackett lines, where we chose  $\beta = 2.5$ , see the text for details.

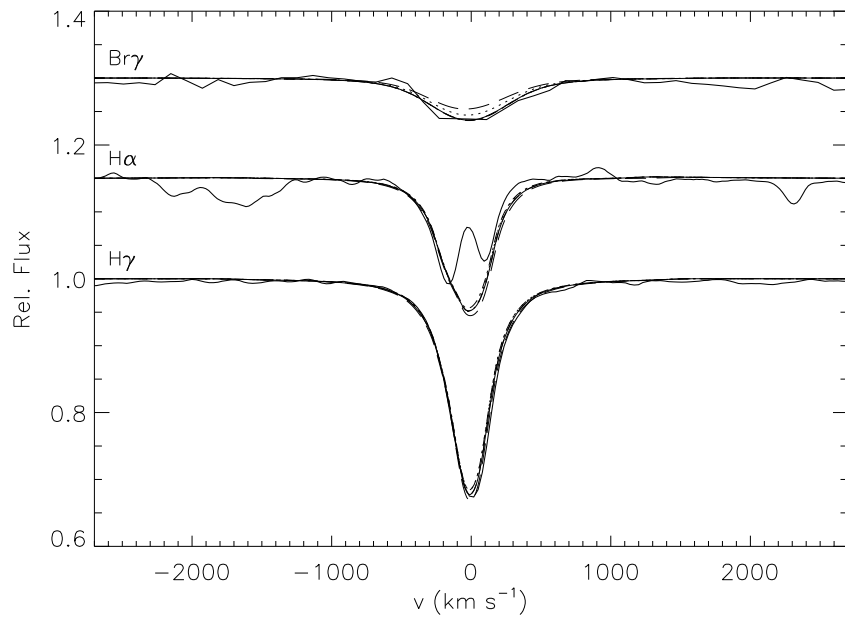


Fig. 14.— Spectrum synthesis for HD 93250 – hydrodynamic/spherical modelling: models A, B, E, F and X (*dotted, dash-dot-dot-dotted, full, dashed and long dashed lines*) and observation (*thick full line*). All computations are performed using a 20-level model atom. Note the nebular emission component in the H $\alpha$  core. For clarity the different spectra are shifted by 0.15 units in ordinate.



Table 3: Effective collision strengths  $\Upsilon_{nn'}$  for the  $n \rightarrow n'$  transitions in H

		T (K)							
$n$	$n'$	2500	5000	7500	10000	15000	20000	25000	30000
1	2	6.40(-1) <sup>a</sup>	6.98(-1)	7.57(-1)	8.09(-1)	8.97(-1)	9.78(-1)	1.06(+0)	1.15(+0)
1	3	2.20(-1)	2.40(-1)	2.50(-1)	2.61(-1)	2.88(-1)	3.22(-1)	3.59(-1)	3.96(-1)
1	4	9.93(-2)	1.02(-1)	1.10(-1)	1.22(-1)	1.51(-1)	1.80(-1)	2.06(-1)	2.28(-1)
1	5	4.92(-2)	5.84(-2)	7.17(-2)	8.58(-2)	1.12(-1)	1.33(-1)	1.50(-1)	1.64(-1)
1	6	2.97(-2)	4.66(-2)	6.28(-2)	7.68(-2)	9.82(-2)	1.14(-1)	1.25(-1)	1.33(-1)
1	7	5.03(-2)	6.72(-2)	7.86(-2)	8.74(-2)	1.00(-1)	1.10(-1)	1.16(-1)	1.21(-1)
2	3	2.35(+1)	2.78(+1)	3.09(+1)	3.38(+1)	4.01(+1)	4.71(+1)	5.45(+1)	6.20(+1)
2	4	1.07(+1)	1.15(+1)	1.23(+1)	1.34(+1)	1.62(+1)	1.90(+1)	2.18(+1)	2.44(+1)
2	5	5.22(+0)	5.90(+0)	6.96(+0)	8.15(+0)	1.04(+1)	1.23(+1)	1.39(+1)	1.52(+1)
2	6	2.91(+0)	4.53(+0)	6.06(+0)	7.32(+0)	9.17(+0)	1.05(+1)	1.14(+1)	1.21(+1)
2	7	5.25(+0)	7.26(+0)	8.47(+0)	9.27(+0)	1.03(+1)	1.08(+1)	1.12(+1)	1.14(+1)
3	4	1.50(+2)	1.90(+2)	2.28(+2)	2.70(+2)	3.64(+2)	4.66(+2)	5.70(+2)	6.72(+2)
3	5	7.89(+1)	9.01(+1)	1.07(+2)	1.26(+2)	1.66(+2)	2.03(+2)	2.37(+2)	2.68(+2)
3	6	4.13(+1)	6.11(+1)	8.21(+1)	1.01(+2)	1.31(+2)	1.54(+2)	1.72(+2)	1.86(+2)
3	7	7.60(+1)	1.07(+2)	1.25(+2)	1.37(+2)	1.52(+2)	1.61(+2)	1.68(+2)	1.72(+2)
4	5	5.90(+2)	8.17(+2)	1.07(+3)	1.35(+3)	1.93(+3)	2.47(+3)	2.96(+3)	3.40(+3)
4	6	2.94(+2)	4.21(+2)	5.78(+2)	7.36(+2)	1.02(+3)	1.26(+3)	1.46(+3)	1.64(+3)
4	7	4.79(+2)	7.06(+2)	8.56(+2)	9.66(+2)	1.11(+3)	1.21(+3)	1.29(+3)	1.34(+3)
5	6	1.93(+3)	2.91(+3)	4.00(+3)	5.04(+3)	6.81(+3)	8.20(+3)	9.29(+3)	1.02(+4)
5	7	1.95(+3)	3.24(+3)	4.20(+3)	4.95(+3)	6.02(+3)	6.76(+3)	7.29(+3)	7.70(+3)
6	7	6.81(+3)	1.17(+4)	1.50(+4)	1.73(+4)	2.03(+4)	2.21(+4)	2.33(+4)	2.41(+4)

		T (K)							
$n$	$n'$	40000	50000	60000	80000	100000	150000	200000	250000
1	2	1.32(+0)	1.51(+0)	1.68(+0)	2.02(+0)	2.33(+0)	2.97(+0)	3.50(+0)	3.95(+0)
1	3	4.64(-1)	5.26(-1)	5.79(-1)	6.70(-1)	7.43(-1)	8.80(-1)	9.79(-1)	1.06(+0)
1	4	2.66(-1)	2.95(-1)	3.18(-1)	3.55(-1)	3.83(-1)	4.30(-1)	4.63(-1)	4.88(-1)
1	5	1.85(-1)	2.01(-1)	2.12(-1)	2.29(-1)	2.39(-1)	2.59(-1)	2.71(-1)	2.81(-1)
1	6	1.45(-1)	1.53(-1)	1.58(-1)	1.65(-1)	1.70(-1)	1.77(-1)	1.82(-1)	1.85(-1)
1	7	1.27(-1)	1.31(-1)	1.34(-1)	1.36(-1)	1.37(-1)	1.39(-1)	1.39(-1)	1.40(-1)
2	3	7.71(+1)	9.14(+1)	1.05(+2)	1.29(+2)	1.51(+2)	1.93(+2)	2.26(+2)	2.52(+2)
2	4	2.89(+1)	3.27(+1)	3.60(+1)	4.14(+1)	4.56(+1)	5.31(+1)	5.83(+1)	6.23(+1)
2	5	1.74(+1)	1.90(+1)	2.03(+1)	2.23(+1)	2.37(+1)	2.61(+1)	2.78(+1)	2.89(+1)
2	6	1.31(+1)	1.38(+1)	1.44(+1)	1.51(+1)	1.56(+1)	1.63(+1)	1.68(+1)	1.71(+1)
2	7	1.17(+1)	1.18(+1)	1.19(+1)	1.19(+1)	1.20(+1)	1.19(+1)	1.19(+1)	1.19(+1)
3	4	8.66(+2)	1.04(+3)	1.19(+3)	1.46(+3)	1.67(+3)	2.08(+3)	2.39(+3)	2.62(+3)
3	5	3.19(+2)	3.62(+2)	3.98(+2)	4.53(+2)	4.95(+2)	5.68(+2)	6.16(+2)	6.51(+2)
3	6	2.08(+2)	2.24(+2)	2.36(+2)	2.53(+2)	2.65(+2)	2.83(+2)	2.94(+2)	3.02(+2)
3	7	1.78(+2)	1.81(+2)	1.83(+2)	1.85(+2)	1.86(+2)	1.87(+2)	1.86(+2)	1.87(+2)
4	5	4.14(+3)	4.75(+3)	5.25(+3)	6.08(+3)	6.76(+3)	8.08(+3)	9.13(+3)	1.00(+4)
4	6	1.92(+3)	2.15(+3)	2.33(+3)	2.61(+3)	2.81(+3)	3.15(+3)	3.36(+3)	3.51(+3)
4	7	1.41(+3)	1.46(+3)	1.50(+3)	1.55(+3)	1.57(+3)	1.61(+3)	1.62(+3)	1.63(+3)
5	6	1.15(+4)	1.26(+4)	1.34(+4)	1.49(+4)	1.63(+4)	1.97(+4)	2.27(+4)	2.54(+4)
5	7	8.26(+3)	8.63(+3)	8.88(+3)	9.21(+3)	9.43(+3)	9.78(+3)	1.00(+4)	1.02(+4)
6	7	2.52(+4)	2.60(+4)	2.69(+4)	2.90(+4)	3.17(+4)	3.94(+4)	4.73(+4)	5.50(+4)

<sup>a</sup> $a(b)$ :  $a \times 10^b$

Table 4. Coefficients of polynomial fits to the bound-free gaunt factors

$n$	$a_1$	$b_1$	$c_1$	$a_2$	$b_2$	$c_2$
1	1.0780	$-8.754(14)^a$	$-1.791(29)$	0.798	$5.358(15)$	$-3.484(31)$
2	1.0926	$-2.019(14)$	$1.836(28)$	0.768	$6.242(15)$	$-3.208(31)$
3	1.0983	$-9.450(13)$	$9.177(27)$	0.793	$5.480(15)$	$-2.318(31)$
4	1.0954	$-5.188(13)$	$3.552(27)$	0.831	$4.094(15)$	$-1.430(31)$
5	1.0912	$-3.200(13)$	$1.576(27)$	0.758	$6.633(15)$	$-3.320(31)$
6	1.0925	$-2.331(13)$	$9.325(26)$	0.790	$5.808(15)$	$-2.844(31)$

Note. —  $a(b)$ :  $a \times 10^b$